Tunneling anomalous Hall effect in nanogranular CoFe-B-Al-O films near the metal-insulator transition

V. V. Rylkov,[1,2,*] S. N. Nikolaev,[1] K. Yu. Chernoglazov,[1] V. A. Demin,[1] A. V. Sitnikov,[3] M. Yu. Presnyakov,[1] A. L. Vasiliev,[1] N. S. Perov,[4] A. S. Vedeneev,[5] Yu. E. Kalinin,[3] V. V. Tugushev,[1] and A. B. Granovsky[2,4]

[1]*National Research Centre "Kurchatov Institute", 123182 Moscow, Russia*

[2]*Institute of Applied and Theoretical Electrodynamics RAS, 127412 Moscow, Russia*

[3]*Voronezh State Technical University, 394026 Voronezh, Russia*

[4]*Faculty of Physics, Lomonosov Moscow State University, 119991 Moscow, Russia*

[5]*Kotel'nikov Institute of Radio Engineering and Electronics RAS, 141190 Fryazino, Moscow Region, Russia*

(Received 18 October 2016; revised manuscript received 2 February 2017; published 12 April 2017)

We present results of an experimental study of structural, magnetotransport, and magnetic properties of a disordered system which consists of the strained crystalline CoFe nanogranules with the size of 2–5 nm embedded into the B-Al-O oxide matrix with a large number of dispersed Fe or Co atoms. They act in the matrix as magnetic ions and contribute essentially to the magnetization at $T \leqslant 25$ K. The conductivity of the system follows the ln$T$ law on the metallic side of the metal-insulator transition in the wide range of metal content variation $x = 49-56$ at. % that formally corresponds to the conductivity of the array of granules with strong tunnel coupling between them. We found that scaling power laws in the dependence of anomalous Hall effect (AHE) resistivity ρ_{AHE} vs longitudinal resistivity ρ strongly differ if temperature T or metal content x are variable parameters. The obtained results are interpreted in terms of the model of two sources of AHE emf arising from metallic nanogranules and insulating tunneling regions, respectively. We suggest that the tunneling AHE component can be caused by the recently predicted scattering assisted mechanism [A. V. Vedyayev *et al.*, Phys. Rev. Lett. **110**, 247204 (2013)] and is strongly shunted due to generation of local circular Hall current.

DOI: 10.1103/PhysRevB.95.144202

I. INTRODUCTION

Even though the anomalous Hall effect (AHE) was first explained in 1954 [1] and intensively studied during recent years [2] several questions on the relative importance and specific features of the basic mechanisms of AHE in different systems are still under strong debate. Nowadays the renewed interest in AHE is related to its common origin with direct and inverse spin Hall effects [3,4], which are key phenomena in spintronics, orbitronics, and magnonics.

The AHE is the most clearly pronounced in magnetic materials (ferromagnetic metals and semiconductors, granular metal-insulator nanocomposites, etc.) with strong spin-orbit interaction (SOI) [2]. Their Hall resistivity ρ_H is described by the sum of two terms,

$$\rho_H = R_0 B + 4\pi R_s M, \tag{1}$$

where the first term describes the normal Hall effect (NHE) induced by the Lorentz force and the second term characterizes the AHE related to SOI; M is the magnetization component perpendicular to the film plane; B is the magnetic induction component in this direction; R_0 and R_s are the so-called NHE and AHE coefficients, respectively.

One of the most interesting lines in the AHE research in magnetic systems is the study of a relation between the anomalous component of the Hall resistivity $\rho_{\mathrm{AHE}} = 4\pi R_s M$ and longitudinal resistivity $\rho_{xx} = \rho$, i.e., the so-called scaling behavior $\rho_{\mathrm{AHE}} \propto \rho^n$, where n is the power-law index determined by one of the other physical mechanisms of the AHE [2]. The scaling relation in this form (or its equivalent for conductivities, $\sigma_{\mathrm{AHE}} = \rho_{\mathrm{AHE}}/\rho^2 = \rho_{\mathrm{AHE}}\sigma^2 \propto \sigma^\gamma$ with $\gamma \approx 2-n$) is widely used in the literature, if impurity concentration or temperature are variable parameters [2]. The simple scaling behavior is well established for homogeneous magnetic systems with the one type of impurity. For example, in low-resistivity magnetic metals with a not very strong impurity scattering $n = 1$ in the case of the skew scattering mechanism, while $n = 2$ in the case of a side-jump or intrinsic mechanism. With increasing of the impurity scattering potential in high-resistivity (so called "dirty") magnetic metallic materials the index n decreases to $n \approx 0.4$ [2,5]. Nevertheless, there are numerous cases when the scaling relation is not maintained and for some heterogeneous systems considerable deviations from the scaling law were reported (see, e.g., [6–9] and references therein).

Rather frequently, interpretation of the AHE data is contradictory and intricate in complex magnetic materials, and most of the investigations of the scaling relation between ρ_{AHE} and ρ were performed for systems which do not exhibit metal-insulator transition (MIT) [2,6–9]. However, some complex structures, in particular, granular nanocomposites—in which it is possible to vary their resistivity by several orders of magnitude (from good metal to insulator) by changing the metal volume fraction—are the most convenient systems for investigation of the scaling relation (if it exists) and other features of the AHE behavior in different metallic and insulating regimes.

To explain experimental results in such structures, Efetov *et al.* [10] considered a theoretical model of densely packed ferromagnetic granules coupled to each other by tunneling contacts in the metallic regime and found that there is no scaling relation between transverse and longitudinal resistivity. In this theory, the AHE regime arises only inside the

*vvrylkov@mail.ru

granules. However, Vedyaev *et al.* showed that the AHE may arise inside tunneling barriers due to the influence of SOI on the scattering of electrons on the intergranular-located impurities [11] or a Rashba spin-orbit coupling within the tunneling barrier layer [12]. Recently, other tunneling AHE (TAHE) mechanisms were considered in Ref. [13], caused by the interfacial SOI which result in a "skew" electron tunneling even in the absence of impurities.

Earlier in [14], the AHE theoretical model was considered for the hopping transport systems: The authors obtained the scaling law with $n = 0.5$ if the impurity concentration is a variable parameter. The basic finding of this theory was that the AHE originates from the influence of SOI on correlated hopping between triads of impurities in the percolation network. That is similar to the NHE in the hopping regime which appears in triads of impurities under the influence of magnetic field on the interference between the amplitude for a direct and indirect (second-order) transition [15]. Detailed calculations of AHE for a hopping between triads of impurities under SOI in the percolation network was carried out in Ref. [16] and scaling with n between 0.67 and 0.24, depending on the specific features of hopping transport, was obtained. However, the above theory of AHE in a percolation network is valid, strictly speaking, only for a hopping regime in diluted systems with isolated magnetic impurities, but not for nanocomposites with densely packed ferromagnetic granules.

An interesting feature of granular nanocomposites consists in unusual behavior of their conductivity near the MIT. It was predicted in [17,18] that in the close vicinity of the MIT on the metallic side when the tunneling conductance between granules G_t is much larger than the quantum conductance $G_q = 2e^2/\hbar$ ($g = G_t/G_q \gg 1$) the conductivity should follow the $\ln T$ behavior ($\sigma \propto \ln T$). Just under these conditions the AHE resistivity ρ_{AHE} does not depend on longitudinal resistivity; i.e., $n \approx 0$ [10]. Recently, such unconventional scaling law with $n \approx 0$ when conductivity follows logarithmic law $\sigma \propto \ln T$ has been demonstrated for Ni-SiO_2 nanocomposites by varying Ni content [19] (in spite of $n \approx 0.6-0.7$ far from the MIT [19,20]). The correlation between ρ_{AHE} and ρ when the temperature is a variable parameter has been not studied in [19].

Parametric dependences of $\rho_{\mathrm{AHE}}(\rho)$ vs T and x have been previously studied in Fe-SiO_2 nanocomposites on the dielectric side of the MIT where the dependence $\ln\sigma \propto (T_0/T)^{1/2}$ comes true [21,22]. It was proved that temperature variation of the $\rho_{\mathrm{AHE}}(\rho)$ dependence follows the power law $\rho_{\mathrm{AHE}} \propto \rho(T)^n$, $n = 0.44-0.59$ [21]. Meanwhile, at the Fe content variation the $\rho_{\mathrm{AHE}}(\rho)$ function revealed strongly nonmonotonic behavior: The Hall effect conductance shows a flattening in the MIT vicinity and a tendency to reach a new plateau at T_0 increasing [22].

The universal scaling factor with $n \sim 0.5$ was observed for p-type insulating $Ga_{1-x}Mn_xAs$($x \sim 0.014$) for films with different hole concentration [23]. On the other hand, in $Ga_{1-x}Mn_xAs$ on the metallic side of the MIT ($x \geqslant 0.05$) the power laws $\rho_{\mathrm{AHE}}(T) \propto [\rho(T)]^2$ and $\rho_{\mathrm{AHE}}(x) \propto [\rho(x)]^{0.5}$ were established at the temperature and Mn content variations, respectively [24]. This difference in the power-law index was explained by a specific dependence of magnetization of a metallic cluster near the MIT on its conductivity; $M \propto \sigma_{xx}^{1.5}$ at low temperatures significantly smaller than the Curie temperature T_C.

Below we present our results on structural, magnetotransport, and magnetic properties of nanogranular CoFe-B-Al-O thin films with excess oxygen vacancies in oxide matrix focusing on scaling relations between Hall resistivity and longitudinal resistivity at $T = 5-200$ K. Note that nanostructures based on oxides such as $AlO_z (z < 1.5)$ possess a resistive switching phenomenon caused by the existence of oxygen vacancies; these phenomena can be used for memristor implementation, synapse simulation, and creation of new types of smart devices [25,26].

Previously it was shown that similar nanocomposites do not exhibit a well-defined percolation threshold [27] and therefore are suitable objects to study AHE in the strongly disordered metallic regime. We consider the metallic regime with the ferromagnetic alloy content $x = 49-56$ at. % close to the MIT when conductivity follows the $\ln T$ behavior and shows that the scaling power law differs if temperature T or content x are variable parameters: $n = 0.4-0.6$, obtained from the temperature variation of ρ and ρ_{AHE} measured for each sample and $n \approx 0.24$, obtained from measurements at fixed low temperature (10–40 K) for samples with different content. We attribute our data to the complex nature of AHE as a result of the action of two parallel emf sources caused by SOI inside the metallic granules and the insulating tunneling barrier between granules.

II. SAMPLES

The nanogranular films under study were produced using the ion-beam sputtering of the composite targets onto glass-ceramic substrates at growth temperature not exceeding 100 °C. The targets include the parent metallic alloy $Co_{40}Fe_{40}B_{20}$ and 12 aluminum oxide (Al_2O_3) plates placed onto the surface of this metal. The special target design makes it possible to obtain composite systems with the relative content of the metallic phase continuously varying ($\delta x = 0.5-0.6$ at. %) in a wide range $x = 25-60$ at. % in a single technological cycle [28]. The films were deposited with the rate of about 0.27 nm/s within ~3 h. The thickness of the produced samples was about $d \approx 2.7\mu$m. The elemental composition of the films was determined by energy dispersive x-ray spectroscopy using an Oxford INCA Energy 250 unit attached to a JEOL JCM-6380 LV scanning electron microscope.

Above we adduce the metal fraction of grown nanocomposite, approximating its structure by the formula $(Co_{40}Fe_{40}B_{20})_x(Al_2O_3)_{100-x}$. We will further use this approximation for the composition characterization because it allows definitely finding the x value by data of energy dispersive x-ray spectroscopy; additionally it gets information about the chemical content of the composition target. On the other hand, the data of structural studies (see below) show that a considerable part of the B atoms in the nanocomposite is appeared to be outside the CoFe granules. The enthalpy of the BO oxide formation (+0.04 eV/molecule) is much less as compared to the enthalpy of the AlO oxide formation (+0.95 eV/molecule) but the binding energy of the BO molecule (8.4 eV) is much larger than that of the AlO molecule (5.0 eV) [29]. For this reason the boron atoms outside the CoFe granules are energet-

ically more favorable to form the BO oxide, while the residual oxygen is more favorable to form $AlO_z (z < 1.5)$ oxide. In the limit when all boron atoms are outside the metal granules the nanocomposite of $(CoFe)_x(BO)_y(AlO_z)_{100-x-y}$ type could be formed. The content of the metal phase herewith decreases. For instance, if in the case of the $(Co_{40}Fe_{40}B_{20})_x(Al_2O_3)_{100-x}$ nanocomposite the x value is ≈50 at. %, then the nanocomposite transformation to $(CoFe)_x(BO)_y(AlO_z)_{100-x-y}$ leads to the $x \approx 40$ at. % and $z \approx 1$.

After producing composites, we used photolithography for preparing the samples having the standard double-cross shape to measure the electrical conductivity and Hall effect resistance. The conduction channel had the width $w = 1.2$ mm and the length $l = 4$ mm, with the distance between potential probes $l_p = 1.4$ mm. The precision of alignment of Hall probes was better than 10 μm.

III. STRUCTURAL CHARACTERIZATION BY ELECTRON MICROSCOPY

The cross-section samples for transmission electron microscopy (TEM) and scanning transmission electron microscopy (STEM) were prepared by a Ga^+ focused ion beam (FIB) in a scanning electron-ion microscope, HeliosNanoLab 600i (FEI, USA) equipped with Pt and W gas injection systems (GIS) and with a micromanipulator, Omniprobe 200. The specimens were studied in a Titan 80-300 TEM/STEM (FEI, USA) with a spherical aberration (C_s probe) corrector at an accelerating voltage of 300 kV. The microscope was equipped with a field emission cathode (Schottky), SuperTwin objective lens with spherical aberration coefficient of 1.2 mm, energy dispersive x-ray (EDX) spectrometer (EDAX, USA), and a high-angle annular dark-field electron detector (HAADF) (Fischione, USA). The EDX microanalysis including elemental mapping was additionally performed in a Tecnai Osiris TEM/STEM (FEI, USA) with attached Super-X EDX system (Bruker, USA) at an accelerating voltage of 200 keV. For the image processing DIGITAL MICROGRAPH (Gatan, USA) software and TIA (FEI, USA) were used.

The HAADF STEM images of samples $(Co_{40}Fe_{40}B_{20})_x(Al_2O_3)_{1-x}$ with $x = 46$ and 57 at. % are presented in Figs. 1(a) and 1(b), respectively. We failed to find a noticeable difference in particle sizes (they lie between $a \approx 2-5$ nm) in these two samples. The selected

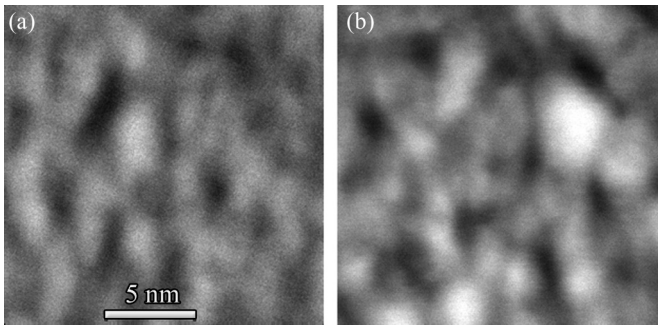

FIG. 1. HAADF STEM images of $(Co_{40}Fe_{40}B_{20})_x(Al_2O_3)_{1-x}$ nanocomposites with (a) $x = 46$ and (b) $x = 57$ at. %. Light areas correspond to Co-Fe metal clusters.

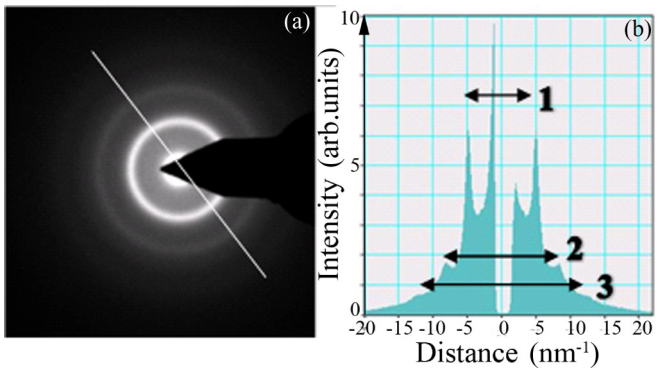

FIG. 2. (a) The selected area electron diffraction (SAED) pattern from a sample with $x = 46$ at. %. (b) Intensity histogram along the white line shown in (a).

area electron diffraction (SAED) pattern from one of the samples is presented in Fig. 2(a) and an intensity histogram along the white line is shown in Fig. 2(b). It demonstrates the peaks correspondent to three interplanar spacings: 2.02, 1.25, and 0.8 Å. These spacings match the distances close to $d(110)$, $d(211)$, and $d(222)$ in a base-entered cubic (bcc) FeCo alloy with unit cell constant $a_c = 0.284\,86$ nm (space group $Im\text{-}3m$) [30]. However, the (200) bcc reflection in our case is absent.

Note that a similar absence of the (200) bcc reflection was observed previously in a Fe-Cr-N alloy after mechanical milling [31], as well as in the study of milled Fe-Cr-X compounds, where X was N, C, and B [32]. After high-resolution transmission electron microscopy (HRTEM) investigations the authors proposed that bow-shaped deformation of the crystal planes of the particles with the size of few nm occurred along the (110) bcc slip planes. Such deformation may cause distortion of the bcc (200) planes and drastic decrease of the (200) reflection. That proposition was confirmed by simulation of the diffraction pattern from the distorted $Fe_{50}Co_{50}$ bcc model consisting of 1000 unit cells [32].

We checked the number of different compounds, including oxides and borides, but all these compounds exhibited the crystal structure with less symmetry; thus the diffraction patterns demonstrate a comparatively large number of peaks. Thus we rule out all these compounds from our consideration.

Close inspection of the SAED pattern, presented in Fig. 2(a), indicates the presence of an amorphous halo which could be linked with the presence of an amorphous oxide substance between the FeCo particles.

Since two samples demonstrated similar microstructure, below we will consider in detail only the specimen with $x = 57$ at. %. As was shown in Fig. 1(b), the HAADF STEM image demonstrated the areas of bright and dark contrast and it can be proposed that the areas with bright contrast correspond to FeCo particles with a high Z number. The areas with the dark contrast could be related to Al and B oxides. To prove that suggestion we performed the EDX mapping and the results are presented in Figs. 3(a)–3(e). There is an unambiguous match of Fe and Co distribution and these areas correspond to the bright areas in the HAADF STEM image. On the contrary, the darker areas correspond to a more intense signal from Al and

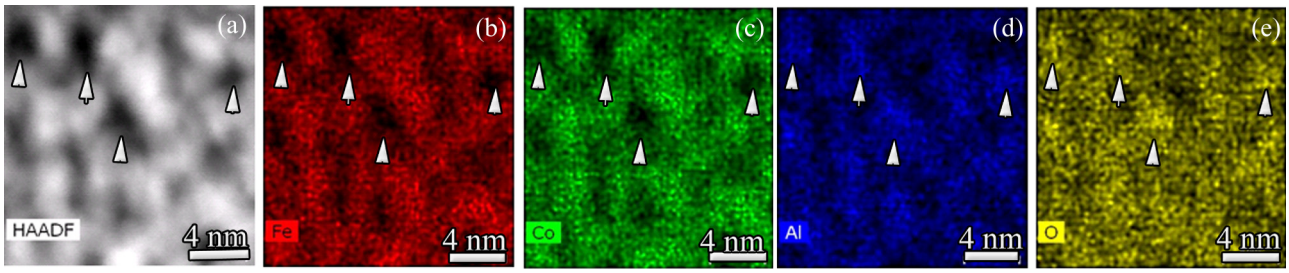

FIG. 3. (a) HAADF STEM image of the sample with $x = 57$ at. % and the elemental maps of (b) Fe, (c) Co, (d) Al, and (e) O. Note the overlapping of Co and Fe elemental distribution in the brighter areas of the image (a) and Al with O in darker areas, which are indicated by arrows.

O; these areas are pointed arrows in Figs. 3(a)–3(e). Boron is the lightest element which can be detected by EDX and the efficiency of B registration is relatively low, so the B elemental map was not informative and we performed the EDX line scan across bright and dark areas (see the bottom of Fig. 4; the scan line is marked by the arrow). Again, the correspondence between Fe and Co on the one hand and Al and O on the other is very clear. The B distribution was not conclusive and it should be studied in more detail with other spectroscopic methods. We only could speculate that B was distributed more or less uniformly both in Fe-Co and Al-O regions with slight excess at the boundaries between them (Fig. 4).

The bright-field (BF) high-resolution STEM (HRSTEM) image of the sample is shown in Fig. 5(a). The lattice image of particles is clearly visible. They are more pronounced in the dark areas, which correspond to FeCo particles. These lattice fringes correspond to the $(110)_{\mathrm{FeCo}}$ crystal planes. Surprisingly, these lattice fringes clearly demonstrate the presence of the texture in relatively large areas, more than 20 nm, which was confirmed by fast Fourier transforms from the HRSTEM images; one of these is shown in Fig. 5(b). The angle between two $\langle 110 \rangle$ maxima was less than 90°, but we attributed that to lattice image distortions during scanning because of charging effects. On the small areas we did observe an image of the crystal planes intersecting under 90° [see enlarged image in Fig. 5(c)]. The BF HRSTEM image of the lattice, obtained from the sample with $x = 46$ at. %, is even more impressive. However, the areas having bright contrast, which correspond to Al (and B) oxides, look more amorphous (not shown here).

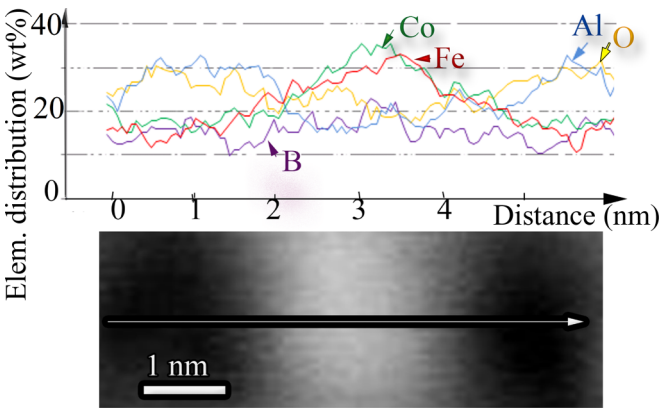

FIG. 4. Fe, Co, Al, O, and B elemental distribution along the arrow shown in the HAADF STEM image in the bottom part.

IV. TRANSPORT AND MAGNETIC PROPERTIES

The investigations of transport properties of nanogranular films were performed using an evacuated insert with a superconducting solenoid, immersed in a liquid-helium Dewar flask. The Hall effect was measured within the 10–200 K temperature range at magnetic fields up to 1.5 T; the conductivity was determined at 6–300 K.

The transversal resistance, $R_{xy} = V_y/I_x$, was measured at various polarities of the magnetic field at "downward" (from $+B$ to $-B$) and "upward" (from $-B$ to $+B$) directions of field scanning. The Hall resistance R_H was determined as an odd component of transversal resistance: $R_H(B) = [R_{xy}(B) - R_{xy}(-B)]/2$. Such an approach makes it possible to distinguish possible hysteresis in the behavior of Hall resistance [33] as well as to suppress the parasitic contribution to R_H from the magnetoresistive effect and incoherent mesoscopic effects caused by reconstruction of a percolation network (percolation paths) at a change of temperature [34] or magnetic field [35,36]. The measurements of field and temperature dependences of the Hall resistance were carried

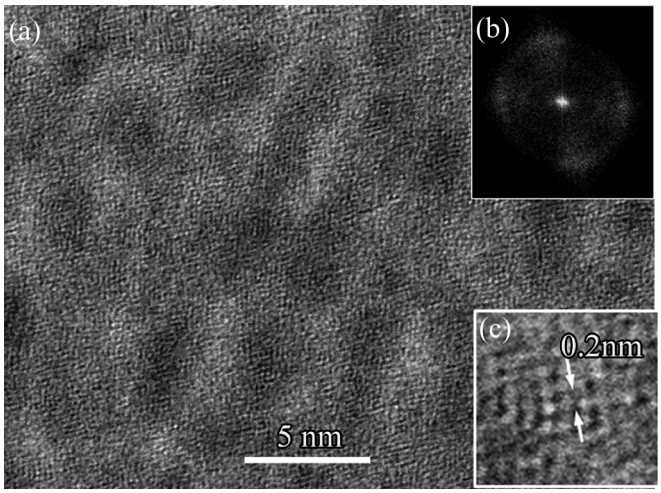

FIG. 5. (a) Bright-field high-resolution STEM image of the sample with $x = 57$ at. %. (b) The FFT from the image. (c) The enlarged image of the sample demonstrating a lattice image with orthogonal $\{110\}$ planes.

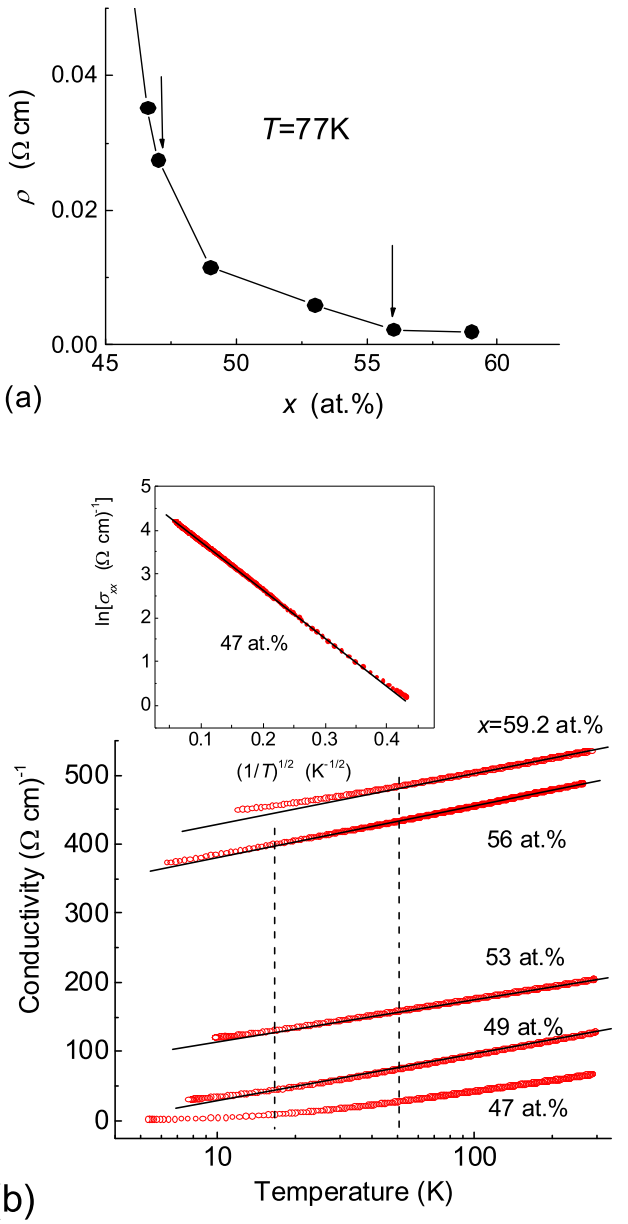

FIG. 6. (a) Resistivity of $(Co_{40}Fe_{40}B_{20})_x(Al_2O_3)_{100-x}$ samples vs ferromagnetic alloy content near the MIT ($x = 46.5-59.2$ at. %) at $T = 77$ K. Arrows show the regions of the MIT ($x_c \approx 47$ at. %) and percolation threshold ($x_p \sim 56-59$ at. %). (b) The temperature dependences of conductivity for samples with different ferromagnetic alloy content $x = 47-59$ at. %.

out in a slow enough mode (within 15 and 40 min, respectively) to exclude the long-term processes of conductivity relaxation in nanogranular composites [36].

The magnetization M measurements were performed with a SQUID magnetometer (Quantum Design PPMS-9T) between 3 and 300 K at in-plane and out-of-plane magnetic fields $\mu_0 H$ up to 5 T.

A. Longitudinal conductivity

The dependence of the resistivity $\rho(x)$ on the content x of $(Co_{40}Fe_{40}B_{20})_x(Al_2O_3)_{100-x}$ samples in the MIT vicinity ($x = 46.5-59.2$ at. %) measured at the temperature $T = 77$ K is shown in Fig. 6(a). The temperature dependence of the longitudinal conductivity $\sigma(T)$ for samples with different x is shown in Fig. 6(b). In linear scale, the resistivity [Fig. 6(a)] starts to increase gradually at $x \leqslant 56$ at. %, while at $x \leqslant 49$ at. % the $\rho(x)$ dependence starts to be exponentially strong. In the range $x = (49-56)$ at. % and $T > (10-15)$ K conductivity is well described by the law $\sigma(T) \propto \ln T$ [Fig. 6(b)] that formally corresponds to the conductivity of metallic granules packed in a regular cubic lattice with strong tunnel coupling between them [17,18]. Note that description of the $\sigma(T)$ dependence by the logarithmic law outside this range (at $x > 56$ at. % and $x < 49$ at. %) is noticeably worse [Fig. 6(b)]. Furthermore, at $x \leqslant x_c \approx 47$ at. % [$\rho_c = (2-3) \times 10^{-2}$ Ω cm] this law changes to $\ln\sigma \propto (T_0/T)^{1/2}$ related to hopping conductivity [see Fig. 6(b), inset] [18]. It means that the MIT in our case occurs near $x_c \approx 47$ at. %. On the other hand, the noticeable deviation from the logarithmic temperature dependence of conductivity is evident already at $x \approx 59$ at. % and the resistivity increases sharply at $x < 56$ at. % [Fig. 6(a)]. It indicates that the percolation threshold probably takes place at $x_p \sim 56-59$ at. %. Note that metallic $Co_{40}Fe_{40}B_{20}$ alloy ($x = 100$ at. %) has the negative coefficient $\alpha = d\rho/dT$ at $T < 300$ K (see, for example, Fig. 6 in [37]). Therefore, in our case other criteria of percolation transition are necessary, compared to nanocomposites of the type of Ni-SiO_2 in which this transition is followed by change of the α sign from the negative to positive as x increases [19].

The probable reason for the percolation transition spreading is due to a nonvanishing conductivity of a dielectric component of the nanocomposite [38]. In our case the conductivity of the bad oxidized B-Al-O matrix can be significant owing to low barriers between granules. For example, under bad oxidized conditions the barrier height can be less than 1 eV in the tunnel junctions type of metal/AlO_x/metal (Me/AlO_x/Me) [39,40]. On the other hand, for optimally oxidized Al-O matrix, the barrier reaches ≈3 eV for Me/AlO_x/Me tunnel junctions [41,42]. Below we focus our attention on the region of compositions with $x = (49-56)$ at. % and resistivity ρ of $10^{-2}-2 \times 10^{-3}$ Ω cm at 77 K, which corresponds to the case of high-resistivity dirty metals [2].

B. Hall effect and magnetization

The magnetic field dependences of the Hall resistance $R_H(B)$ for samples with $x = 47$, 49, and 59 at. % at low temperatures ($T < 25$ K) are shown in Fig. 7(a). The character of the presented $R_H(B)$ dependences is similar to the ones observed in ferromagnetic films with easy-plane magnetic anisotropy. Note that in nanocomposite samples with activation type of conductivity, when AHE is determined by superparamagnetic granules, the $R_H(B)$ curve transforms into a "rounded" Langevin function [21]. In our case the AHE resistance $R_{AHE}(B) \approx R_H(B)$ linearly increases with the field up to $B \leqslant B_s$ and then saturates at $B \geqslant B_s$ (B_s is the field of saturation magnetization M; we considered that $R_0 \ll R_s$ because it is a common feature for magnetic granular systems [19–21]). Figure 7(b) demonstrates the $R_H(B)$ dependences measured for the sample with $x \approx 56$ at. % at various

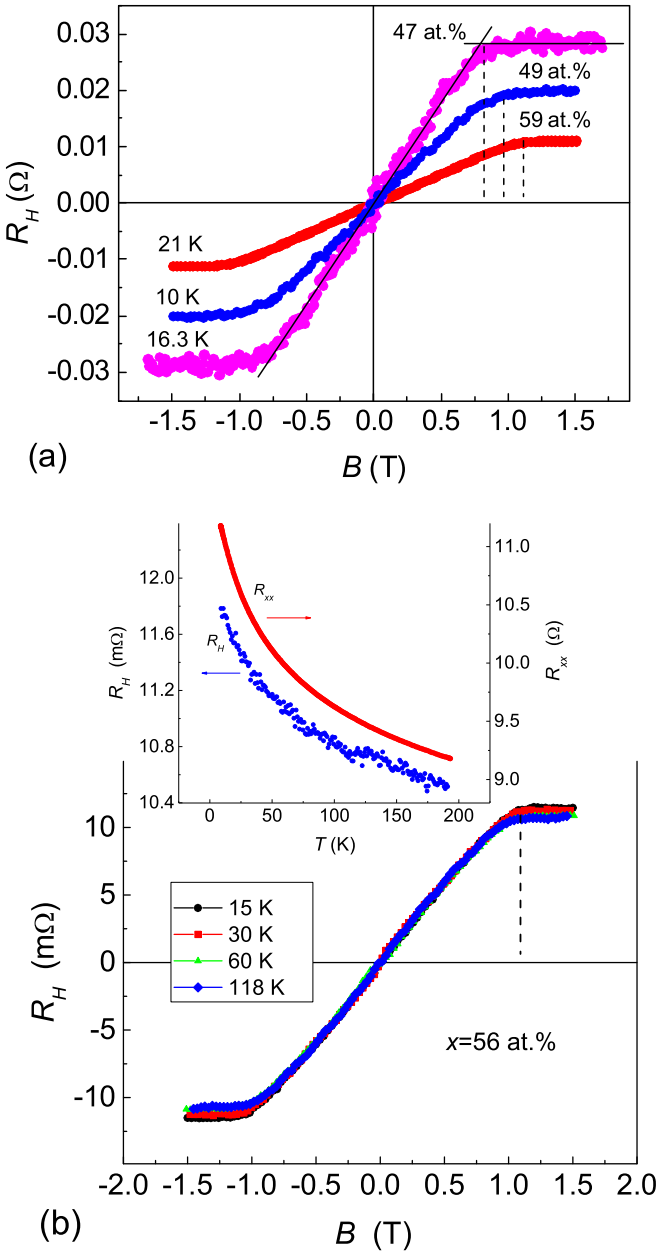

FIG. 7. (a) Magnetic field dependences of the Hall resistance $R_H(B)$ for samples with $x = 47, 49$, and 59 at. % at low temperatures $T < 25$ K. (b) Dependence of $R_H(B)$ for sample with $x = 56$ at. % within the 15–120 K temperature range. Inset shows the temperature dependences of $R_H(T)$ and longitudinal resistance $R_{xx}(T)$ measured at $B = 1.5$ T for this sample.

temperatures in the range of 15–120 K. In this temperature range the saturation field B_s practically does not depend on temperature. Moreover, good correlation in temperature behavior of the Hall resistance $R_H(T)$ and longitudinal resistance $R_{xx}(T)$ measured at $B = 1.5$ T is observed; the $R_H(T)$ and $R_{xx}(T)$ increasing with temperature lowering from 190 to 9 K are 1.12 and 1.26 times, respectively [see Fig. 7(b), inset].

Usually, both the AHE conductivity σ_{AHE} and resistivity ρ_{AHE} are linear functions of the magnetization $M(x,T)$ that need to be considered at the scaling relation studies. The temperature dependence of $M(T)$ measured at 1.5 T is strong at 5–20 K and $M(T)$ very weakly decreases with increase of temperature at $T \geqslant 25$ K [Fig. 8(a)]. This behavior is probably because of a large number of paramagnetic Co and Fe atoms in the oxide B-Al-O matrix and superparamagnetic granules belonging to the dead ends of the percolation cluster [43,44]. Note that the data of structural measurements also indicate the presence of a large number of Co and Fe atoms in the oxide matrix (Fig. 4). Following percolation theory (see Chaps. 5 and 12 in [43,44], respectively) we present the topological scheme of percolation cluster [see Fig. 8(a), inset], which includes a conductive network or "cluster skeleton" (red lines), a large number of the dead ends (black lines), and isolated Fe-Co atomic inclusions (black points). The skeleton is created in our case by tunnel coupled CoFe nanogranules. The feature of the percolation system is that its conduction near the percolation threshold is determined by the skeleton. Meanwhile magnetization of such a system near the threshold is mainly controlled by the "black" phase [43,44]. We will discuss this model with more details specific for our case in the following section.

Figure 8(b) shows the magnetic field dependences of magnetization for samples with $x = 49$ and 56 at. %, measured in the field perpendicular and parallel to the plane at different temperatures in the range of 3–200 K. At temperatures <25 K the paramagnetic phase with dispersed Fe or Co impurities is clearly observed in the total magnetization of samples. The magnetization of this phase is saturated at 3 K in the field higher than 3T. On the other hand, the saturation field B_s for the magnetization of the ferromagnetic phase associated with granules does not practically depend on the temperature in the studied temperature region. The out-of-plane saturation field of this phase is $B_s \approx 1$ T which well correlates with the Hall effect data (Fig. 7).

At $T \geqslant 25$ K the magnetization $M(x,T)$ is practically independent of T in comparison with the resistance $\rho(T)$ [Fig. 8(c)]. Due to this reason, one could neglect the $M(x,T)$ temperature variation and assume that the $\rho_{\mathrm{AHE}}(T)$ dependence is mainly determined by the $\rho(T)$ dependence. Also notice that the $M(x,T)$ variation with the metal content in the range of $x = (49-56)$ at. % should not be large. Below, analyzing the scaling dependence ρ_{AHE} vs $\rho(x)$, we will fit the $M(x,T)$ dependence on the metal content in this range by a linear function of x.

The dependence of the AHE conductivity σ_{AHE} on the longitudinal conductivity σ_{xx} at $B = 1.5$ T for samples with $x = 49$, 53, and 56 at. % at different temperatures is shown in Fig. 9. The obtained index $\gamma = 1.55-1.61$ for samples with $x = 49-53$ at. % near the MIT is very close to the widely accepted value $\gamma = 1.6$ (or $n = 0.4$) for dirty metals with $\rho \geqslant 10^{-4}$ Ω cm [2,5]. On the other hand, for samples with $x = 56$ at. % the corresponding value is $\gamma = 1.41$ or $n \approx 0.6$, which coincides with $n \approx 0.6-0.7$ for Ni-SiO_2 nanocomposites far from the MIT [19,20]).

Surprisingly, the power-law index n in the $\rho_{\mathrm{AHE}}(x)/x \propto \rho(x)^n$ relation decreases to sufficiently low value $n \approx 0.24$ if the metal content x is a variable parameter (Fig. 10). Note that in this case the n value is practically independent of the temperature at $T < 40$ K and drops down to $n \approx 0.20$ at $T \approx 160$ K (see Fig. 10, inset).

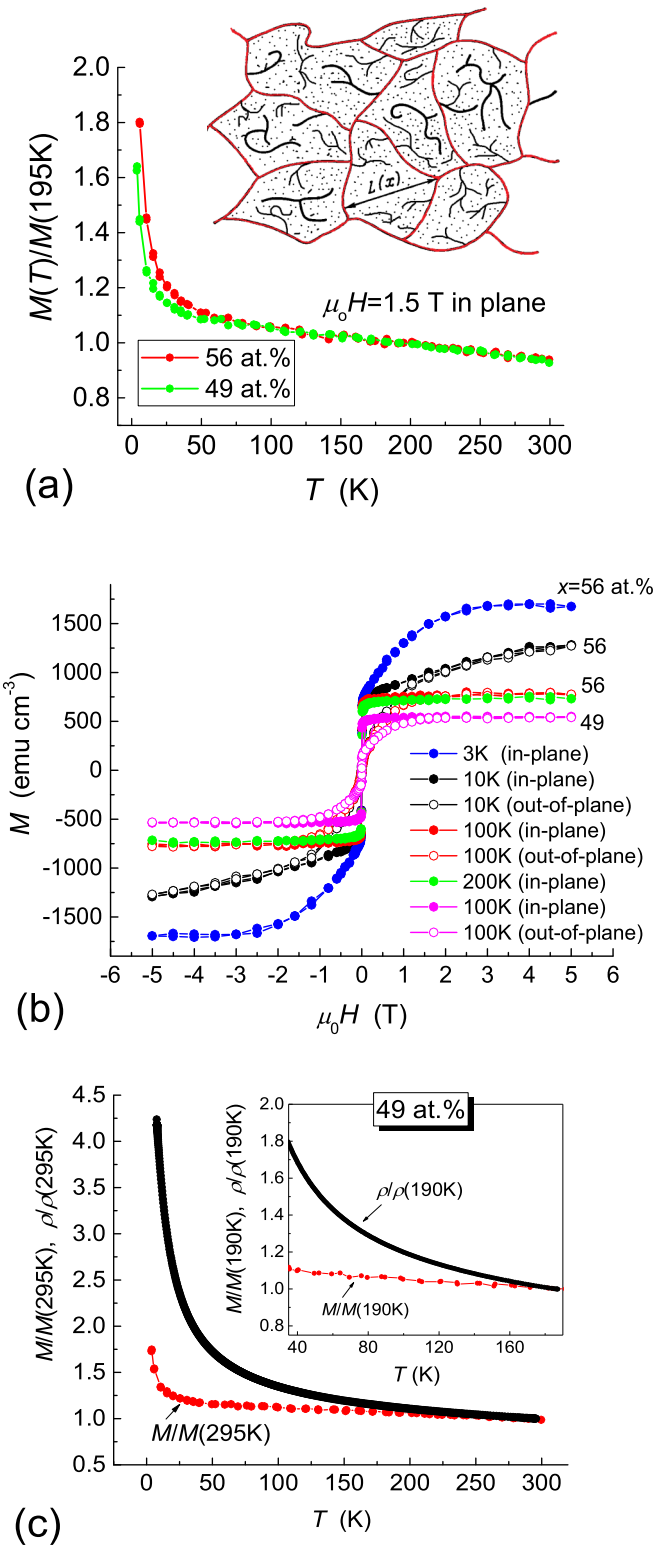

FIG. 8. (a) Temperature dependences of normalized magnetization M for $(Co_{40}Fe_{40}B_{20})_x(Al_2O_3)_{100-x}$ films with $x = 49$ and 56 at. %. Inset demonstrates the topological scheme of the percolation cluster including conductive network or "cluster skeleton" (red lines) formed by tunnel coupling CoFe nanogranules, the dead ends (black lines), and isolated atomic Fe-Co inclusions (black points). L is the correlation length of the percolation network. (b) Magnetic field dependences of the film magnetization $M(B)$ measured at in-plane and out-of-plane magnetic fields for different temperatures: at 100 K for a sample with 49 at. % and at 3, 10, 100, and 200 K for a sample with 56 at. %. (c) Normalized $M(T)$ dependence in comparison with normalized resistivity $\rho(T)$ dependence for sample with $x = 49$ at. %. Inset shows the normalized $M(T)$ and $\rho(T)$ dependences in the enlarged temperature scale ($T \approx 30$–190 K).

V. DISCUSSION

Before presenting a qualitative model of the AHE in the studied films, let us make several remarks about a specific characteristic of our system provided by its strong heterogeneity.

A. Remarks on the longitudinal conductivity

The above presented conductivity results for CoFe-B-Al-O nanocomposites based on strongly nonstoichiometric oxide show a relatively broad percolation threshold spreading region near the MIT vicinity, $\delta x_p = (x_p - x_c) \sim 7$ at. % [Fig. 6(a)]. In this region, experimental temperature dependence of the conductance σ is well fitted by the logarithmic function: $\sigma = \sigma_0 + \beta \ln T$, where σ_0 and β are the fitting parameters. This dependence is typical for a granular metallic system at large tunnel conductance between granules and not very low temperature [17,18], when weak localization effects are suppressed. The physical origin of this dependence is not connected with the system dimension, but is only due to renormalization of the Coulomb interaction by impurity scattering processes, which affects the quasiparticle tunneling between granules [17,18].

Estimation of the percolation threshold region for Ni-SiO_2 nanocomposites based on stoichiometric oxide gives, however, the much lower value of $\delta x_p = (x_p - x_c) \sim 1$ at. % [19]. From this dissimilarity we can suppose a significant role of the oxide matrix in the conductivity of our system caused by the existence of oxygen vacancies (bad matrix oxidation) leading the low-energy (less than 1 eV) tunneling barriers between metallic grains to appear. That is a typical situation for the metal/AlO_x/metal tunnel junctions containing bad oxidized AlO_z regions ("hot spots") with an effective tunneling area of about $0.1-1\ \mu m^2$ [39,40] which strongly exceeds in our case the granule cross section (percolation network).

Another peculiarity of our CoFe-B-Al-O nanocomposites is a very small variation of the slope β in the logarithmic temperature dependence of the conductanceσ when the metal content x is varied in the percolation threshold spreading region, $x = (49-56)$ at. % [see Fig. 6(b)]. In contrast to the Ni-SiO_2 system, where β has a change of $\sim$2 times at $\delta x_p \sim 1$ at. % [19], in our case $\beta = 26-32(\Omega\,\mathrm{cm})^{-1}$ at $\delta x_p \sim 7$ at. %. According to the model [17,18], below the percolation threshold when $g = G_t/(2e^2/\hbar) > 1$, where g and G_t are, respectively, normalized and non-normalized tunneling conductance, the conductivity of the nanocomposite with granules packed in an arbitrary periodic lattice follows the law

$$\sigma(T) = \sigma_0\left(1 - \frac{1}{2\pi D g}\ln\left[\frac{g E_c}{k_B T}\right]\right) = \sigma_0\left(1 - \frac{1}{\pi k g}\ln\left[\frac{g E_c}{k_B T}\right]\right). \quad (2)$$

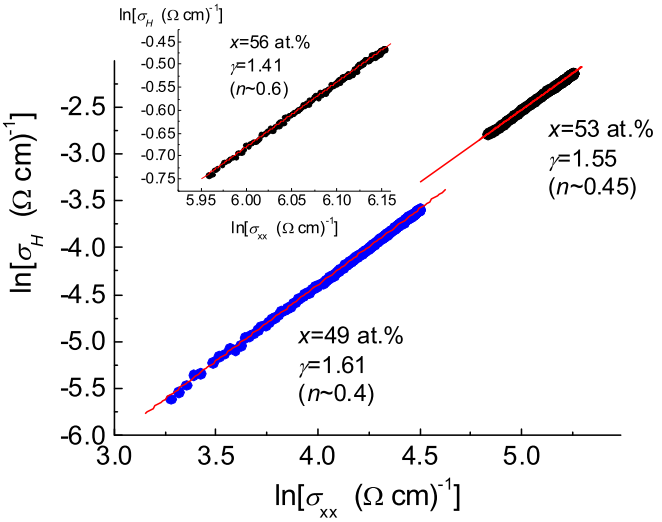

FIG. 9. Logarithmic plots of AHE conductivity σ_{AHE} vs σ_{xx} for samples with $x = 49$ and 53 at. %. Inset shows the $\sigma_{\mathrm{AHE}}(\sigma_{xx})$ dependence for sample $x = 56$ at. %.

Here D is the system dimension, k is the coordination number of the periodic lattice (or the number of granule contacts with the nearest neighbors), and E_c is the Coulomb energy. The formula (2) is correct at $g\delta \ll T \ll E_c$, where δ is the mean energy level spacing in a single granule. The connection between the fitting parameter β and the model parameters in (2) is evident: $\beta = \sigma_0(1/\pi kg)$.

The applicability of (2) to the case of an irregular array of granules, like our nanocomposite, is discussed in [18] (see p. 486). It is expected that in three-dimensional (3D) samples the conductance dispersion effect on macroscopic transport is less important than in 2D or 1D ones; it is expected also that the

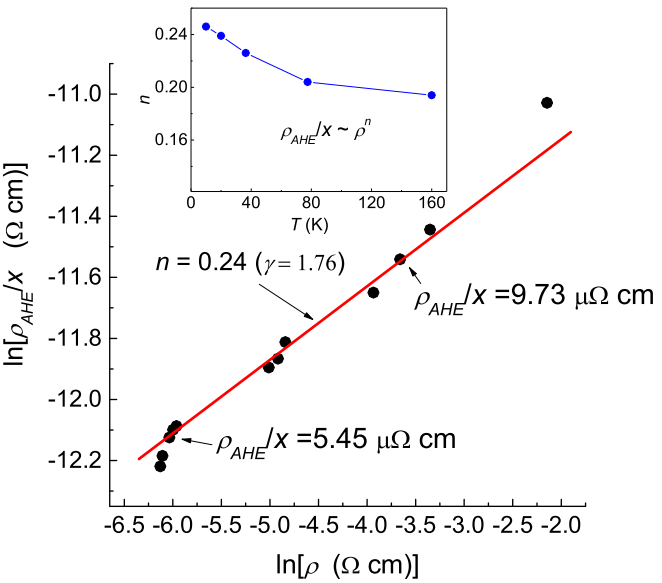

FIG. 10. Logarithmic dependence of normalized AHE resistivity (ρ_{AHE}/x) vs longitudinal resistivity ρ, obtained from measurements at a fixed low temperature in the range of 10–36 K for samples with different metal content x. Inset shows the temperature dependence of power-law index n in the $\rho_{\mathrm{AHE}}(x)/x \propto \rho(x)^n$ scaling relation.

k value in Eq. (2) is determined by an effective coordination number of neighbors of a granule in percolation paths.

According to the percolation conductivity model the parameter σ_0 is connected with the tunneling conductance G_t by the relation $G_t \approx i\sigma_0(L^2/L) = i\sigma_0 L$ [43,44]. It leads to the following expression:

$$\sigma_0 \approx \frac{2e^2 g}{\hbar i L}, \tag{3}$$

where L is the correlation length of the percolation network or its "lattice constant" [see Fig. 8(a), inset]; i is the effective number of tunnel junctions on the correlation length ($i \sim L/a$). Substituting of Eq. (3) into Eq. (2) gives

$$\beta[(\Omega\,\mathrm{cm})^{-1}] = \frac{2e^2}{\hbar\pi ki L} = 1.55 \times 10^{-4}\,(kiL[\mathrm{cm}])^{-1}. \tag{4}$$

In the case of metal-insulator type systems, the L value is weekly dependent on the metal content x in the percolation threshold spreading region [38]. According to the data of Fig. 6 the x decreasing actually means in our system an effective increasing of the intergranular distance b and also a decreasing of the tunneling conductance G_t at about constant correlation length L. The typical number of granule contacts k in the percolation network is equal to 2–3 near the percolation threshold [43,44]. Substituting $i = 2, k = 2{-}3$ and the experimentally obtained slope value $\beta \approx 29(\Omega\,\mathrm{cm})^{-1}$ into (4) leads to the value of $L \approx 9$–13 nm that significantly exceeds the granule size $a = 2{-}5$ nm estimated from the electron microscopy results (Fig. 1). It testifies to the validity of the used model of conductivity near the percolation threshold, since under these conditions the inequality $L \gg a$ has to be carried out [43,44].

B. Remarks on the magnetization

During analysis of the correlation between magnetization and AHE data (Figs. 7 and 8) a serious problem arises from a complex character of distribution of magnetic atoms between different components of the nanocomposite, i.e., metallic FeCo granules and Al-B-O matrix with dispersed Fe and Co ions. Really, according to the percolation theory, near the percolation threshold only a very small part of the metallic granules participates in the conducting cluster or percolation network, while the main "mass" of granules is concentrated in the dead ends and is useless for electrical conductivity. Nevertheless, just this part determines the total magnetization of the system [44]. Presuming that the structure of the percolation network and dead ends is identical, a certain correlation in the total magnetization and AHE behaviors should be expected. However, such correlations can be strongly broken, for example, at a larger deposition rate of the nanocomposite film as in our case when the considerable part of the metal fraction appears in an atomic (ion) phase in the dielectric matrix. (Probably the same situation takes place in the case of NiFe-SiO_2 nanocomposites grown by magnetron cosputtering (the film thickness of ≈ 1 μm) [45] in which a sufficiently large value of critical metal volume fraction for the percolation transition $x_{pv} \approx 0.6$ is observed; the theoretical value $x_{vp} \approx 0.25{-}0.3$ [43]).

We attribute a strong increase in magnetization (almost double) at low temperature to the effect of magnetic moments ordering of Fe and Co impurities inside Al-B-O matrix. It is clearly seen from the $M(B)$ curve at 3 K of Fig. 8(b) that their paramagnetic contribution to total magnetization is about 10^3 emu/cm^3. Since for isolated Fe^{3+} ions the moment $m = 5.9\mu_B$, and for Co^{2+} $m = 4.8\,\mu_B$ [46], we can roughly estimate that the concentration of magnetic centers is about $n_i \sim 10^{22}\,\mathrm{cm}^{-3}$.

C. Qualitative model of the AHE behavior

The peculiarities of the magnetotransport properties of our system clearly manifest themselves in the anomalous Hall effect measurements and cannot be adequately described by a one-component Hall-source model. The principal difficulty of such a simplified description is due to the complex character of SOI scattering of electrons by the magnetic centers inside and outside the granules, which drives transverse conductivity in our nanocomposite. On the one hand, the statement seems evident that the metal contribution V_{Hg} to the Hall emf caused by the granules themselves [10] exists in the system. This contribution is due to the SOI scattering of spin-polarized electrons by the magnetic centers inside the granules while the tunneling between them may be described by the same manner as for longitudinal conductivity, i.e., introducing some effective tunnel integral. But such the simplest manner of description is unsuccessful in the presence of the second magnetic phase, i.e., magnetic ions dispersed outside metallic granules (in the tunnel barriers) and having charge and spin configurations different from the ones existing inside the metallic granules. These ions can participate in the SOI processes with the electrons already spin polarized inside metallic granules, so additional contribution to the Hall emf may be noticeable due to a strong SOI integral [11].

Conditions for the appearance of metallic conductance $g = G_t/(2e^2/\hbar) > 1$ could be fulfilled even at relatively large distances between metallic granules, $b \sim 1$ nm, if the tunneling barriers are sufficiently low ($\leqslant$1 eV). In this situation, the tunneling contribution V_{Hd} to the Hall emf may arise due to the TAHE mechanism [11]. Following Ref. [11], the V_{Hd} value is determined by the electron spin polarization inside metallic electrodes (in our case metallic granules), the SOI integral of electrons with impurity scattering centers, and the concentration of these centers, n_i. Since the centers with SOI scattering coexist in both metallic and insulating parts of the system, a one-component picture of the Hall emf in an effective magnetic material becomes incorrect and below we try to qualitatively describe AHE in the model of a two-component structure, containing two coexisting contributions, V_{Hg} and V_{Hd}, to the the Hall emf.

In our experiments, the Hall emf is measured at 1.5 T in the temperature range above ~25 K where the magnetization is almost constant and provided by the granules. However, magnetization increases strongly below ~25 K, and we attribute this fact to the alignment of individual Co and Fe impurity moments in the tunnel barriers. That means that above 25 K at 1.5 T these moments are randomly oriented, but this magnetic impurity disorder does not affect TAHE since the tunneling electron spin polarization is only due to the granules' magnetization, following the model [11]. In particular, it is manifested in a weak dependence of index n vs T (see Fig. 10, inset).

Let us consider a simple phenomenological model with two Hall emf sources connected in parallel with one another [Fig. 11(a)]. A similar situation takes place in a macroscopic rectangular semiconductor sample [47,48], where the circular Hall current occurs in the vicinity of metallic electrodes [Fig. 11(b); a is the size of the cube form metallic granule which plays the role of a metallic electrode in our case]. That leads to the Hall emf shunting effects or a reduction of the potential drop V_H measured between Hall probes as compared to the Hall emf arising in the interelectrode regions, $V_{Hd} = R_{Hd} I_x$.

For a sample with $b/a \leqslant 1/2$ the measured value of the Hall resistance, $R_H = V_H/I_x$ can be estimated on the base of an equivalent circuit model taking into account the combined influence of two Hall emf sources connected in parallel [see Fig. 11(c)]. Figure 11(c) illustrates an effective Hall emf generator for a periodic net of tunnel junctions, which contains: (i) the source of Hall emf in metallic granules, $V_{Hg} = R_{Hg} I_x$, with internal resistance $r_{\mathrm{gint}} = V_{Hg}/I_{sc}$; I_{sc} is the short-circuit current through the granule; and (ii) the source of Hall emf in dielectric intergranular regions, $V_{Hd} = R_{Hd} I_x$, with internal resistance $r_{\mathrm{dint}} \gg r_{\mathrm{gint}}$. These sources are connected in parallel with each other through external resistance $r_{\mathrm{dext}} \gg r_{\mathrm{gint}}$. The effective Hall emf generator [see Fig. 11(c)] generates the Hall emf. $V_{\mathrm{Heff}} = V_H$, which we find using Kirchhoff's circuit laws:

$$2V_H = [(\varphi_{d1} - \varphi_{d0}) + (\varphi_{g1} - \varphi_{g0})] = A + B,$$
$$A \approx V_{Hd}\frac{r_{\mathrm{dext}}}{(r_{\mathrm{dint}} + r_{\mathrm{dext}})};\quad B \approx V_{Hg}\frac{(2r_{\mathrm{dint}} + r_{\mathrm{dext}})}{(r_{\mathrm{dint}} + r_{\mathrm{dext}})}. \qquad (5)$$

The term A in (5) is determined by TAHE and according to [47,48] $A = V_{Hd} f(b/a)$. For a sample with $b/a \leqslant 1/2$, $f(b/a) \cong 0.74 \times (b/a)$ (see Fig. 2 and Table 1 in [47,48], respectively); i.e., $r_{\mathrm{dext}}/r_{\mathrm{dint}} \approx 0.74 \times (b/a)$. Under these conditions, $r_{\mathrm{dint}} \gg r_{\mathrm{dext}}$, and the term B in (5) caused by AHE in granules, is $B \approx 2V_{Hg}$. So, at $b/a \leqslant 1/2$ we have $V_H \approx 0.37(b/a)V_{Hd} + V_{Hg}$, or

$$\rho_{\mathrm{AHE}}(x,T) = R_H(x,T)d \approx [0.37(b/a)R_{Hd} + R_{Hg}]d$$
$$= 0.37(b/a)\rho_{Hd}(x,T) + \rho_{Hg}(T), \qquad (6)$$

where $\rho_{Hd}(x,T)$ and $\rho_{Hg}(T)$ are the TAHE and granule AHE resistivities, respectively. Recall that according to [10,19] the last term in (6) does not depend on x. The factor 0.37 (b/a) reducing the component $R_{Hd}(x,T)$ in Eq. (6) reflects an aforementioned shunting of the local TAHE sources in our percolation system; at small change of metal fraction x below some value $x_0 \leqslant x_p$, i.e., at $\Delta x = (x_0 - x) \ll x_0$, the variation of $b/a \propto \Delta x/x_0$.

Obviously, in the frame of this phenomenological approach we cannot specify the $R_{Hd}(x,T)$ behavior as a function of x and T. The theory of TAHE was developed only at $T = 0$ K and for a tunnel junction with flat ferromagnetic electrodes of a large area, but not for nanogranular array. Besides, the value of the TAHE coefficient depends on a number of the model parameters, such as barrier height, width, and shape, all of which can be different in disordered systems. Therefore, we are unable to average Eq. (6) over tunneling barriers distribution. For this

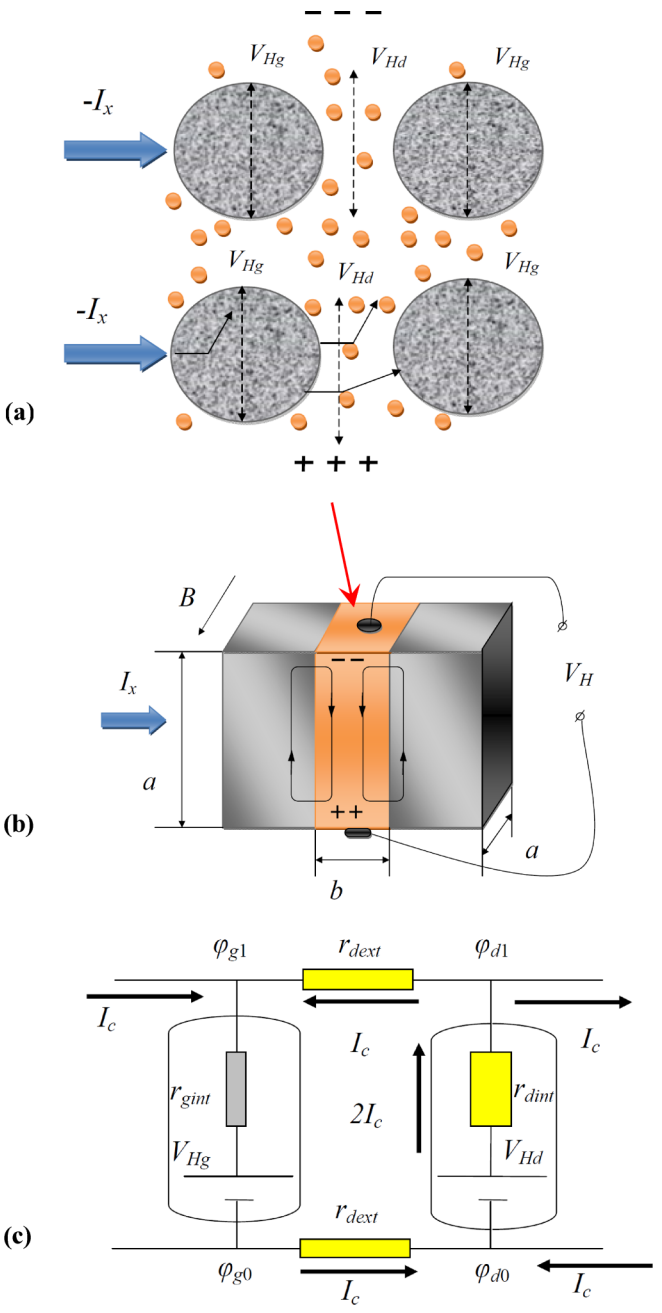

FIG. 11. (a) Granular system with SOI scattering on defects in oxide matrix at electron tunneling between grains. Two connected in parallel sources of AHE emf are shown: the first source is caused by spin-orbit interaction in granules ($V_{Hg} = R_{Hg} I_x$) and the second occurs inside the tunneling barrier regions ($V_{Hd} = R_{Hd} I_x$); the current I_x flows through the neighboring granules; R_{Hg} and R_{Hd} are the Hall resistances of granules and dielectric interlayer between them. (b) Schematic drawing of the tunneling junction between granules illustrating an emergence of circular currents at formation of the Hall effect in the dielectric interlayer. (c) Equivalent scheme of a periodic network of tunnel junctions (resistances) with the two local Hall emf generators; $r_{\text{dint}} \gg r_{\text{dext}} \gg r_{\text{gint}}$, $V_{\text{Heff}} = \frac{1}{2}[(\varphi_{g1} - \varphi_{g0}) + (\varphi_{d1} - \varphi_{d0})]$.

reason, below in our speculative description we will rely on the principal idea of the microscopic model of TAHE exposed in Ref. [11]. Apparently, the TAHE contribution becomes particularly significant below the percolation threshold and therefore one can expect the scaling between AHE resistivity and the longitudinal one with index $n \neq 0$, which is really the case (Fig. 10). The $\Delta\rho_{\text{AHE}}$ vs Δx dependence obtained for the low-temperature region, $T \leqslant 25$ K, is shown in Fig. 12 for $x_0 = 56$ at. %. This dependence can be fitted by the power law with exponent ≈2 that also can be considered as evidence of TAHE. Note that TAHE resistivity grows with increasing Δx when magnetization of the ferromagnetic component falls [Fig. 8(b)]. It is explained that the TAHE according to [11] is determined by local magnetization of granules, but not magnetization of the granular array.

We consider the results presented in Figs. 10 and 12 as a manifestation of the TAHE contribution in the total AHE near the MIT. The main reason for the AHE increase with the metal content decrease is caused by *a creation of* TAHE *sources in the percolation granular network.* It is important that TAHE signal appears against the background of sufficiently large AHE component from granules (see Fig. 10) which does not depend on x below the percolation transition. It is the main reason for the small index $n \approx 0.24$ in the $\rho_{\text{AHE}}(x)/x \propto \rho(x)^n$ dependence.

Another situation takes place in the scaling relation $\rho_{\text{AHE}}(T) \propto \rho(T)^n$ at the change of temperature for the fixed metal content. In this case tunnel probability does not depend (or very slightly depends) on the temperature (see [11]). Since the granule size is small (2–5 nm) one can expect very strong scattering by their interfaces and therefore the temperature behavior of the corresponding contribution $R_{Hg}(T)$ to $R_H(x,T)$ is similar to that observed in very thin metal film [8]. A large number of dispersed magnetic impurity centers inside the tunneling barriers, possible ferromagnetic order between their magnetic moments, the spin-flip processes—all these factors form the temperature dependence of AHE in studied systems. As a result for a sample with $x = 56$ at. % (far from the MIT) we observe the value of $\gamma \approx 1.4$ or $n \approx 0.6$ that coincides with $n \approx 0.6 - 0.7$ for Ni-SiO_2 nanocomposites

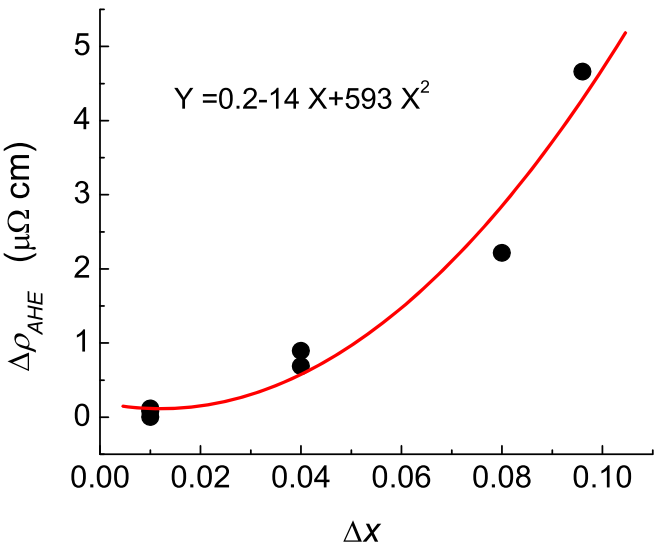

FIG. 12. Variation of AHE resistivity $\Delta\rho_{\text{AHE}}$ vs $\Delta x = (x_0 - x)$ at $T \leqslant 25$ K for $x_0 = 56$ at. %.

above the percolation threshold [19,20]). On the other hand, the obtained index $\gamma \approx 1.6$ for a sample with $x = 49$ at. % near the MIT is the same as for one-phase magnetic materials with high resistivity ($\rho \geqslant 10^{-4}\,\Omega\,\mathrm{cm}$) studied in [5,49]. This coincidence perhaps is not accidental and is probably due to the fact that strong scattering and localization effects manifested in our granular system near the MIT also play an important role in scaling the $\sigma_{\mathrm{AHE}} \propto \sigma^{\gamma}$ relation of dirty magnetic conductors [5,49].

VI. CONCLUSION

We considered the metallic regime of the CoFe-B-Al-O nanocomposites with the metal content $x = 47-59$ at. % in its formula approximation $(Co_{40}Fe_{40}B_{20})_x(Al_2O_3)_{100-x}$. We showed that the relation between the AHE resistivity $\rho_{\mathrm{AHE}}(T,x)$ and longitudinal resistivity $\rho(T,x)$ does not follow the universal scaling law, if T or x are variable parameters: $\rho_{\mathrm{AHE}}(T) \propto \rho(T)^{0.4-0.6}$ ($\gamma = 1.4-1.6$), obtained from the temperature variation of ρ and ρ_{AHE} measured for each sample at fixed x and $\rho_{\mathrm{AHE}}(x)/x \propto \rho(x)^{0.24}$ ($\gamma = 1.76$), obtained from measurements at a fixed low temperature (10–40 K) for samples with different x. We explain our data by a strongly heterogeneous character of our system, which manifested itself in the existence of two types of magnetic component (metallic granules and magnetic centers outside the metallic granules), sufficiently small-height insulating barriers between metallic granules, and SOI scattering processes of electrons both in the granules and on the dispersed magnetic impurities in the barriers. This heterogeneity leads to the TAHE mechanism in the barriers accompanying an ordinary AHE mechanism provided by metallic granules. Based on the magnetization and structural measurements, we give preference to the theoretically predicted scattering assisted TAHE mechanism [11].

ACKNOWLEDGMENTS

This work was financially supported by the Russian Science Foundation, Grant No. 16-19-10233. The work was partially done on the equipment of the Resource Center of Kurchatov Institute Complex of NBICS technologies. The authors acknowledge partial support from M. V. Lomonosov Moscow State University Program of Development for magnetic measurements.

[1] J. M. Luttinger, Phys. Rev. **112**, 739 (1958).
[2] N. Nagaosa, J. Sinova, S. Onoda, A. H. MacDonald, and N. P. Ong, Rev. Mod. Phys. **82**, 1539 (2010).
[3] A. Hoffman, IEEE Trans. Magn. **49**, 5172 (2013).
[4] J. Sinova, S. O. Valenzuela, J. Wunderlich, C. H. Back, and T. Jungwirth, Rev. Mod. Phys. **87**, 1213 (2015).
[5] S. Onoda, N. Sugimoto, and N. Nagaosa, Phys. Rev. Lett. **97**, 126602 (2006); Phys. Rev. B **77**, 165103 (2008).
[6] A. V. Vedyaev, A. B. Granovskii, and O. A. Kotel'nikova, *Transport Phenomena in Disordered Ferromagnetic Alloys* (Moscow State University, Moscow, 1992) (in Russian).
[7] A. V. Vedyaev, A. B. Granovsky, A. V. Kalitsov, and F. Brouers, J. Exp. Theor. Phys. **85**, 1204 (1997).
[8] Y. Tian, L. Ye, and X. Jin, Phys. Rev. Lett. **103**, 087206 (2009).
[9] D. Hou, G. Su, Y. Tian, X. Jin, S. A. Yang, and Q. Niu, Phys. Rev. Lett. **114**, 217203 (2015).
[10] H. Meier, M. Y. Kharitonov, and K. B. Efetov, Phys. Rev. B **80**, 045122 (2009).
[11] A. Vedyayev, N. Ryzhanova, N. Strelkov, and B. Dieny, Phys. Rev. Lett. **110**, 247204 (2013).
[12] A. V. Vedyayev, M. S. Titova, N. V. Ryzhanova, M. Y. Zhuravlev, and E. Y. Tsymbal, Appl. Phys. Lett. **103**, 032406 (2013).
[13] A. Matos-Abiague and J. Fabian, Phys. Rev. Lett. **115**, 056602 (2015); T. H. Dang, H. Jaffrès, T. L. Hoai Nguyen, and H.-J. Drouhin, Phys. Rev. B **92**, 060403(R) (2015).
[14] A. V. Vedyaev and A. B. Granovsky, Sov. Phys. Solid State **28**, 1293 (1986).
[15] T. Holstein, Phys. Rev. **124**, 1329 (1961).
[16] X.-J. Liu, X. Liu, and J. Sinova, Phys. Rev. B **84**, 165304 (2011).
[17] K. B. Efetov and A. Tschersich, Phys. Rev. B **67**, 174205 (2003).
[18] I. S. Beloborodov, A. V. Lopatin, V. M. Vinokur, and K. B. Efetov, Rev. Mod. Phys. **79**, 469 (2007).
[19] D. Bartov, A. Segal, M. Karpovski, and A. Gerber, Phys. Rev. B **90**, 144423 (2014).
[20] A. Pakhomov, X. Yan, and B. Zhao, Appl. Phys. Lett. **67**, 3497 (1995).
[21] B. A. Aronzon, D. Yu. Kovalev, A. N. Lagarkov, E. Z. Meilikhov, V. V. Rylkov, M. A. Sedova, N. Negre, M. Goiran, and J. Leotin, JETP Lett. **70**, 90 (1999).
[22] B. A. Aronzon, A. B. Granovskii, D. Yu. Kovalev, E. Z. Meilikhov, V. V. Rylkov, and M. V. Sedova, JETP Lett. **71**, 469 (2000).
[23] S. Shen, X. Liu, Z. Ge, J. K. Furdyna, M. Dobrowolska, and J. Jaroszynski, J. Appl. Phys. **103**, 07D134 (2008).
[24] X. Liu, S. Shen, Z. Ge, W. L. Lim, M. Dobrowolska, J. K. Furdyna, and S. Lee, Phys. Rev. B **83**, 144421 (2011).
[25] J. J. Yang, D. B. Strukov, and D. R. Stewart, Nat. Nanotechnol. **8**, 13 (2012).
[26] M. Prezioso, F. Merrikh-Bayat, B. D. Hoskins, G. C. Adam, K. K. Likharev, and D. B. Strukov, Nature **521**, 61 (2015).
[27] Yu. O. Mikhailovsky, D. E. Mettus, A. P. Kazakov, V. N. Prudnikov, Yu. E. Kalinin, A. S. Sitnikov, A. Gerber, D. Bartov, and A. B. Granovsky, JETP Lett. **97**, 473 (2013).
[28] Yu. E. Kalinin, A. N. Remizov, and A.V. Sitnikov. Phys. Solid State **46**, 2146 (2004).
[29] L. B. Gurvich, G. B. Karachevtsev, V. N. Kondrat'ev, Yu. A. Lebedev, V. A. Medvedev, V. K. Potapov, and Y. S. Khodeev, *Energy of Chemical Bond Rupture, Ionization Potentials and Electron Affinity* (Nauka, Moscow, 1974) (in Russian).
[30] W. C. Ellis and E. S. Greiner, Trans. Am. Soc. Met. **29**, 415 (1941).
[31] T. Fukunaga, E. Ishikawa, and U. Mizutani, J. Jpn. Soc. Powder Powder Metall. **38**, 324 (1991).
[32] T. Yamasaki, S. Kanatani, and Y. Ogino, in *Structure of Fe-Cr-X (X = N, C and B) Powdered Allow Prepared by Mechanical Milling, In Advanced Materials '93: Computations, Glassy Materials, Microgravity and Non-Destructive Testing,* edited by

T. Masumoto, M. Doyama, K. Kiribayashi, and T. Kisi (Elsevier, Amsterdam, 1994), pp. 93–96.

[33] V. V. Rylkov, B. A. Aronzon, Y. A. Danilov, Yu. N. Drozdov, V. P. Lesnikov, K. I. Maslakov, and V. V. Podolskii, J. Exp. Theor. Phys. **100**, 742 (2005); V. V. Rylkov, S. N. Nikolaev, K. Y. Chernoglazov, B. A. Aronzon, K. I. Maslakov, V. V. Tugushev, E. T. Kulatov, I. A. Likhachev, E. M. Pashaev, A. S. Semisalova, N. S. Perov, A. B. Granovskii, E. A. Gan'shina, O. A. Novodvorskii, O. D. Khramova, E. V. Khaidukov, and V. Y. Panchenko, JETP Lett. **96**, 255 (2012).

[34] B. Raquet, M. Goiran, N. Nègre, J. Léotin, B. Aronzon, V. Rylkov, and E. Meilikhov, Phys. Rev. B **62**, 17144 (2000).

[35] B. A. Aronzon, A. A. Likalter, V. V. Rylkov, A. K. Sarychev, M. A. Sedova, and A. E. Varfolomeev, Phys. Status Solidi B **205**, 151 (1998); V. V. Rylkov, B. A. Aronzon, A. S. Lagutin, V. V. Podol'skii, V. P. Lesnikov, M. Goiran, J. Galibert, B. Raquet, and J. Léotin, J. Exp. Theor. Phys. **108**, 149 (2009).

[36] V. V. Rylkov, B. A. Aronzon, A. B. Davydov, D. Yu. Kovalev, and E. Z. Meilikhov, J. Exp. Theor. Phys. **94**, 779 (2002).

[37] G. V. Swamy, P. K. Rout, M. Singh, and R. K. Rakshit, J. Phys. D: Appl. Phys. **48**, 475002 (2015).

[38] B. I. Shklovskii, Sov. Phys. JETP **45**, 152 (1977).

[39] L. S. Dorneles, D. M. Schaefer, M. Carara, and L. F. Schelp, Appl. Phys. Lett. **82**, 2832 (2003).

[40] E. S. Cruz de Gracia, L. S. Dorneles, L. F. Schelp, S. R. Teixeira, and M. N. Baibich, Phys. Rev. B **76**, 214426 (2007).

[41] H. Boeve, E. Girgis, J. Schelten, J. De Boeck, and G. Borghs, Appl. Phys. Lett. **76**, 1048 (2000).

[42] J. Nowak, D. Song, and E. Murdock, J. Appl. Phys. **87**, 5203 (2000).

[43] B. I. Shklovskii and A. L. Efros, *Electronic Properties of Doped Semiconductors* (Springer-Verlag, New York, 1984).

[44] A. L. Efros, *Physics and Geometry of Disorder: Percolation Theory (Science for Everyone)* (Mir Publishers, Moscow, 1986), *Fizika I Geometriia Besporiadka* (Moscow, Nauka, 1982), Russian version available at http://www.math.ru/lib/files/pdf/kvant_19.pdf.

[45] A. B. Pakhomov and X. Yan, Solid State Commun. **99**, 139 (1996).

[46] C. Kittel, *Introduction to Solid State Physics*, 4th ed. (John Wiley & Sons Inc., New York, 1971).

[47] I. Isenberg, B. R. Russell, and R. F. Greene, Rev. Sci. Instrum. **19**, 685 (1948).

[48] J. Volger, Phys. Rev. **79**, 1023 (1950).

[49] T. Fukumura, H. Toyosaki, K. Ueno, M. Nakano, T. Yamasaki, and M. Kawasaki, Jpn. J. Appl. Phys. **46**, L642 (2007).